Role of vorticity distribution in the rise and fall of lift during a transverse gust encounter

Antonios Gementzopoulos,* Girguis Sedky, and Anya Jones
Department of Aerospace Engineering, University of Maryland, College Park, Maryland 20742, USA

(Received 2 August 2023; accepted 15 December 2023; published 18 January 2024)

The prediction of gust loads during atmospheric flight can aid in the design, assessment and certification of aircraft, and can also enhance the reliability of low-inertia vehicles which are susceptible to large atmospheric disturbances. In this paper, we explore how the vorticity distributions shed from a wing's leading and trailing edges affect its lift history during a large-amplitude transverse gust encounter. Emphasis is placed on comparing experimental lift transients and vorticity distributions with those predicted by Küssner's transverse gust model. Wings with both sharp and blunt leading edges are towed through a vertical jet in a water towing tank to simulate the wing-gust encounter. It is observed that while the quasisteady circulation of Küssner's model increases, its lift prediction provides a good first-order approximation of the experimental lift transient across a large range of gust ratios and Reynolds numbers. The success of the inviscid model is traced to its ability to capture the circulatory characteristics of the viscous separated flow. Its performance deteriorates in the latter phases of the encounter, when the quasisteady circulation decreases. This is shown to be due to a fundamental difference in the lift reduction mechanism between the model and the experiments, resulting in contrasting shed vorticity distributions. Namely, the lift drop-off in the model is governed by the delayed response to a negative change in its quasisteady bound circulation, while in the experiments it is governed by the detachment of the leading-edge vortex and the persistent shedding of negative circulation into the wake.

DOI: 10.1103/PhysRevFluids.9.014701

I. INTRODUCTION

Calculating the forces on a body immersed in a fluid is a fundamental problem in fluid mechanics with important engineering applications. In aeronautics, calculation of the static and dynamic loads produced by an aircraft flight surface is an essential aspect of flight vehicle design. The governing equations of fluid motion are, in general, extremely difficult to solve. Aerodynamicists have instead resorted to either numerical simulations of the governing equations, also known as computational fluid dynamics (CFD), or to simplified fluid flow models that can be solved analytically or numerically. Specifically, the use of potential flow, which assumes an inviscid, irrotational, incompressible fluid, has been successful at predicting the aerodynamic lift on wings at low angles of attack, serving as the foundation of what is known as classical aerodynamics [1]. Its success can be traced to the observation of Prandtl [2], who postulated that viscous forces are negligible except close to solid boundaries, where the no-slip condition needs to be satisfied. Through a simplification of the governing equations, Prandtl showed that the pressure is approximately uniform across a boundary layer and, thus, for attached flows at high Reynolds numbers, potential flow is able to approximate the pressure distribution on a lifting surface [3]. Experimental data have shown that this holds true

*ageme@umd.edu

for both steady and unsteady flows, as long as the flow remains attached, and the vorticity shed from the trailing edge is accounted for [3–6].

At high angles of attack, lifting surfaces exhibit trailing- or leading-edge separation, and the boundary layer arguments which justified the use of potential flow are no longer valid. This is manifested in the inability of potential flow to predict the reduction in the steady-state lift slope that occurs at high angles of attack. Unsteady potential flow lift predictions suffer the same shortcomings several convective times after an initial unsteady forcing—say, a large step change in the angle of attack [7]. However, during the initial transient, researchers have observed that wings are able to sustain lift values close to the potential flow prediction [7–13]. This phenomenon, often called delayed stall, is a well-known characteristic of separated flows and is facilitated by the formation of a leading-edge vortex (LEV). As described by McCroskey [14], a growing LEV attached to the wing delays stall at high angles of attack, which allows for higher instantaneous lift coefficients than would otherwise be possible under steady conditions. The LEV detachment process marks the end of lift enhancement and the inception of stall. Flows encompassing LEVs have been studied extensively due to their prevalence in the unsteady locomotion of biological fliers and swimmers [15,16].

The accuracy of unsteady potential flow models outside the domain of their validity can be perhaps explained through the concept of fluid impulse. In the absence of nonconservative forces, the fluid impulse is an invariant of the flow, despite any unsteadiness [17]. Thus, any forces on an immersed body can be calculated from the change in fluid impulse, which can be computed as a moment of the flow vorticity field [18],

$$\boldsymbol{I} = \frac{1}{n_d - 1}\left(\int_{V_f} \boldsymbol{x} \times \boldsymbol{\omega} \mathrm{d}V + \int_{S_b} \boldsymbol{x} \times (\hat{\boldsymbol{n}} \times \boldsymbol{u}) \mathrm{d}S\right),$$
$$\boldsymbol{F} = -\rho \frac{\mathrm{d}\boldsymbol{I}}{\mathrm{d}t}, \tag{1}$$

where n_d denotes the number of dimensions, V_f is the fluid volume, S_b is the solid surface with unit normal vector $\hat{\boldsymbol{n}}$, $\boldsymbol{x}$ is the spatial coordinate, and $\boldsymbol{u}$ and $\boldsymbol{\omega}$ are velocity and vorticity vector fields, respectively. Caution must be used when applying this equation to experimental data because it only applies to unbounded domains. Thus, it is possible that vorticity that is located outside an experimental field of view can influence the body forces. The second integral in (1) vanishes under the conditions that the reference frame is fixed to the body, and that this body frame is inertial. Lift can then be expressed as the change in vertical fluid impulse,

$$L = -\rho \frac{\mathrm{d}}{\mathrm{d}t} \int_{V_f} x \omega_z \mathrm{d}V. \tag{2}$$

Equation (2) shows that lift can be explicitly computed from the generation of vorticity and its streamwise movement. It has been recently demonstrated that, in many cases, potential theory correctly predicts the development of both circulatory and noncirculatory vortex sheets [19,20], which can be experimentally isolated using standard results of potential theory [21]. Hence, even if potential flow models require the use of erroneous assumptions, they can still approximate lift transients by capturing the hydrodynamic impulse of viscous separated flows. Furthermore, vortex-impulse can be used to augment models using data from experiments or simulations. Notably, Babinsky *et al.* [9] used the above ideas to develop a low-order model for pitching and surging wings. They found that Wagner's model [5] accurately predicted the lift of pitching and surging wings when the relative advection of vortices is properly accounted for. Polet *et al.* [22] used similar ideas to estimate the force on a wing undergoing a perching maneuver. Ōtomo *et al.* [23] found that Theodorsen's pitch model performs remarkably well despite the formation of a LEV, and the discrepancy in lift after the LEV detaches can be accounted for using the relative advection of the LEV with the circulation in the wake. Stevens and Babinsky [24] found that the LEV circulation as calculated from experimental measurements of a pitching wing closely follows the bound circulation

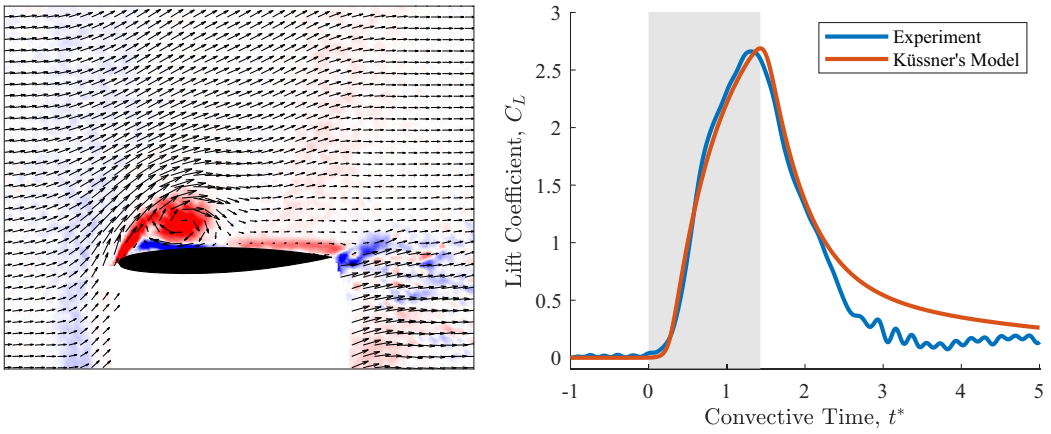

FIG. 1. Example experimental transverse gust encounter measurements: (a) vorticity and velocity field and (b) experimental lift transient compared with Küssner's model.

predicted by Wagner's model, suggesting that the lift is dominated by the circulatory component regardless of whether a leading-edge vortex is formed or not. Furthermore, the work of Ford and Babinsky [10] showed that, for an impulsively started airfoil at high angle of incidence, most of the vorticity in the flow is not in the bound vortex but shed in the wake.

Küssner's transverse gust encounter model has also been reported to agree with experimental data for a wide range of gust ratios and gust profiles [25–27]. This model is the focus of the current work, as there has been a recent effort to understand the physics of gust mitigation and to design new gust alleviation strategies [28,29]. In the past, models of varying fidelity have been used to predict force transients produced during gust encounters, including unsteady potential flow [30], state-space formulations [31], and experimental, data-driven models [32]. However, Küssner's model has several enticing properties. Its computational simplicity makes it a great candidate for online control applications. Moreover, Küssner's model is based on well-understood physics, and its agreement with data suggests that it can be used to understand the different force producing mechanisms during a gust encounter [33]. Defining the gust ratio to be the ratio of peak gust velocity to freestream velocity, i.e., $GR = V/U_\infty$, and the gust-width-to-chord ratio (w/c) to be the streamwise width of the gust divided by the chord, Fig. 1 depicts an example flowfield and lift transient for a transverse gust encounter with a trapezoidal gust profile, $GR = 0.75$, and $w/c = 1.4$. The gray area denotes the convective times that the leading edge is in the gust. The flow is massively separated at the leading edge (and therefore not potential), the wake is deflected due to the gust velocity, and the gust vorticity is deformed. However, the predictive ability of Küssner's model shown in Fig. 1(b) suggests that the model is able to capture some essential aspects of the encounter. One of the goals of this paper is to identify the mechanisms by which this inviscid model is able to predict the lift transients of viscous, separated flows, and explore its limitations.

All unsteady potential flow models mentioned above have a known limitation: They overpredict force transients after LEV detachment. The concept of the optimal vortex formation introduced by Gharib *et al.* [34] and extended to unsteady airfoil kinematics by Dabiri [35] can be used to estimate the timescale of LEV detachment. It describes the nondimensional period of time over which a single vortex created by a vortex generator grows. Its maximal value denotes the time that the vortex stops entraining fluid from the shear layer and detaches. Optimal vortex formation is defined as $\hat{T} = C\Gamma/(D\Delta U)$, where Γ is the instantaneous circulation of the vortex, C is a constant depending on the configuration, D is the characteristic length scale of the flow, and ΔU is the velocity difference across the shear layer feeding the vortex. Dabiri [35] showed evidence that there is a universal

optimal formation time $\hat{T} \approx 4$ in vorticity-driven lift and propulsion. However, subsequent research revealed that this is not always true [36,37]. The variation in optimal vortex formation time has been attributed to differing LEV detachment mechanisms. Two competing mechanisms governing LEV detachment have been identified: the bluff body detachment mechanism and the boundary layer eruption mechanism [38]. The former is associated with the interaction of the LEV with the trailing edge of the wing. The latter is associated with the vortex-wall interaction between the LEV and the airfoil surface. A characterization of the relevant vortex detachment parameters can be found in Kissing *et al.* [39].

Given the demonstrated importance of the LEV, another goal of this paper is to analytically investigate its growth during a gust encounter. The seminal work of Didden [40] expressed the growth rate of a vortex by integrating the vorticity flux over the shear layer. By assuming a linear velocity profile across the shear layer, the vorticity can be approximated by

$$\omega_z \approx \frac{\mathrm{d}u}{\mathrm{d}y} \approx \frac{\Delta U}{\delta},$$

where δ is the thickness of the shear layer feeding the vortex. The approximation is shown in equation (3). Similarly, the size of the LEV can be approximated by the mass flux from the shear layer into the vortex. Written in terms of nondimensional quantities, the results for circulation and area of a vortex are shown in equations (4) and (5), respectively, where $t^* = tU_\infty/c$ is the convective time:

$$\Gamma(t) = \int_0^t \int_0^\delta u\omega_z \mathrm{d}y\mathrm{d}\tau = \int_0^t \int_0^\delta u\frac{\mathrm{d}u}{\mathrm{d}y}\mathrm{d}y\mathrm{d}\tau \approx \frac{1}{2}U_\infty^2 t, \tag{3}$$

$$\frac{\Gamma(t^*)}{cU_\infty} = \frac{t^*}{2}, \tag{4}$$

$$A(t) = \int_0^t \int_0^\delta u\mathrm{d}y\mathrm{d}\tau \approx \frac{1}{2}U_\infty \delta t,$$

$$\frac{A(t^*)}{c^2} = \frac{\delta t^*}{2c}. \tag{5}$$

Widmann and Tropea [38] used the above results along with a Falkner-Skan approximation for the boundary layer thickness δ to investigate the vortex detachment mechanisms of a plunging airfoil. Rival *et al.* [41] and Sattari *et al.* [42] used a similar approximation to study the growth of starting vortices and the effects of leading-edge geometry on LEV growth and detachment.

It is important to note that this paper considers wings with a geometric angle of attack of 0° as Küssner's model is formulated this way. Thus, the effect of upward and downward gusts is identical, which is in general not true and care must be taken to account for additional effects. Furthermore, this paper considers the prediction of lift and not pitching moment. Küssner's model predicts that the lift always acts through the quarter-chord, which is in clear disagreement with the well-known suction peak that propagates down the chord of the wing with the LEV. Thus, it is expected that the moment coefficient between the inviscid model and the experiment will be different. Furthermore, finite wing effects are not considered in this work and will be the subject of future research. It is believed that the tip vortex has a small influence on the flow early in the gust encounter. This can be justified based on the following intuition: (1) The full wing tip only enters the gust at a convective time of 1, (2) the wing tip vortex does not extend to infinity but only starts at gust entry.

The objectives of this study are (i) to investigate the effect of the shed leading-edge and trailing-edge vorticity distributions on the lift experienced by a wing during a transverse gust encounter, (ii) to make an in-depth comparison between viscous and inviscid gust encounters. The organization of the paper is as follows: Section II presents the experimental setup, Küssner's model, and the vorticity flux methods used in the paper. Section III A presents the general flow and lift characteristics. Section III B investigates the scaling of the LEV growth during a gust encounter.

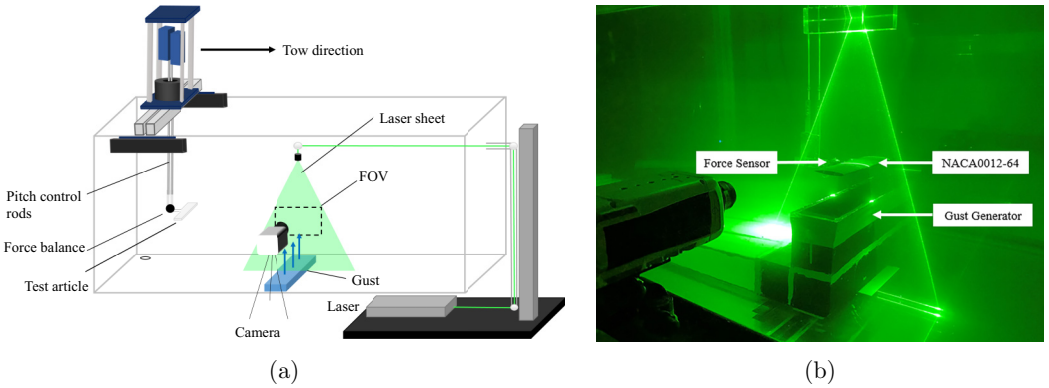

FIG. 2. Experimental apparatus at the University of Maryland water towing tank depicting (a) the tow tank configuration (b) the wing and its instrumentation during a transverse gust encounter.

Section III C analyzes the experimental shed vorticity distributions and compares them to Küssner's inviscid model. Finally, Sec. III D discusses the vortex detachment timescales for transverse gust encounters.

II. METHODOLOGY

A. Experimental methods

Experiments were carried out in The University of Maryland (UMD) free-surface water towing tank shown in Fig. 2. The tank dimensions are 7 m long, 1.5 m wide, and 1 m deep. The tank is equipped with a four-degree-of-freedom model motion system, allowing for streamwise, stream normal, and pitching motions. The freestream was created by towing the wing through the tank, and a transverse gust was created via a planar jet flow. Two gust generation systems can be interchanged to produce two different gust profiles: A sine-squared gust profile and a trapezoidal gust profile, depicted in Fig. 3(a). Details on the gust system design and profiles can be found in Ref. [43].

This paper presents data from two separate experimental campaigns: (i) A flat plate wing encountering a sine-squared gust, (ii) and a NACA0012-64 wing encountering a trapezoidal gust.

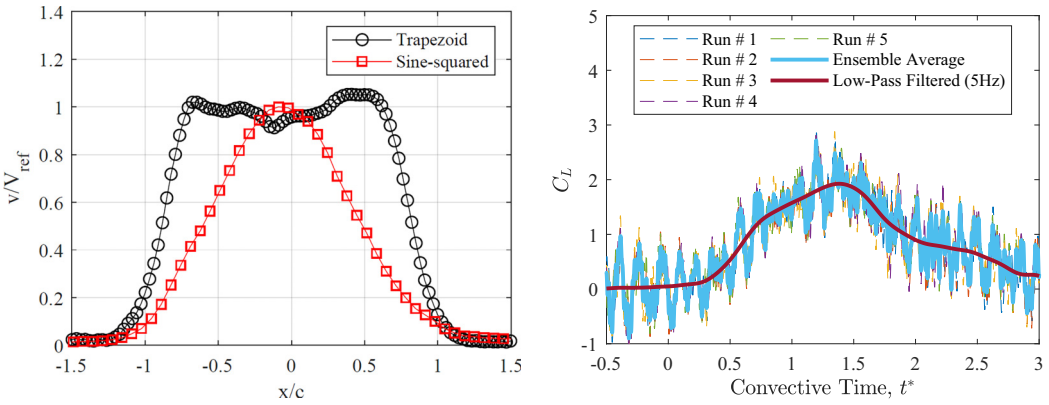

FIG. 3. (a) Time-averaged gust velocity profiles generated by the UMD towing tank gust generator. Figure obtained from Ref. [43] with permission. (b) Example of an unfiltered, ensemble averaged, and low-pass filtered lift signal obtained using the ATI Mini-40 force balance.

TABLE I. Experimental test matrix

Gust profile	Gust ratio	Maximum incidence	Reynolds number
Trapezoidal	0.75	37°	6000, 12 000
Trapezoidal	0.50	27°	12 000, 17 000
Trapezoidal	0.30	17°	12 000, 28 000
Trapezoidal	0.20	11°	12 000, 42 000
Sine-squared	1.50	56°	20 000
Sine-squared	1.00	45°	20 000
Sine-squared	0.75	37°	20 000
Sine-squared	0.50	27°	20 000

The purpose of using data from different experiments is not to make a direct comparison between them but to take advantage of the different frames of reference the experiments were conducted in. Notably, the flat plate experiments took advantage of the tow particle image velocimetry (PIV) capability of the UMD tank, where the camera and laser sheet were towed with the wing model. Thus, the PIV data are in the frame of reference of the model and all shed vorticity is captured. The flat plate was made from brass and has a chord of 7.62 cm and a span of 30.48 cm, resulting in an aspect ratio of 4 and a 0.043 thickness-to-chord ratio. The experiments were conducted at a Reynolds number of 20 000 and the gust width-to-chord ratio was 2.6. More details on the flat plate experiments can be found in Ref. [44].

The NACA0012-64 wing used has a chord of 10.5 cm and a span of 63 cm, resulting in an aspect ratio of six. The gust width-to-chord ratio was calculated to be 1.4. The velocity vector fields were measured using static PIV in which the laser and the camera are fixed in the laboratory reference frame. A laser sheet was created in the vicinity of the gust, using a Quantel Evergreen Nd:YAG 532 nm laser, as shown in Fig. 2(b). The water tank was seeded with class IV soda lime spheres with 37 μm diameter. The images were taken 2.5 chords away from the wing tip. A Phantom v641 camera with 2560 × 1600 pixel resolution was used to capture images at 15 Hz in the laboratory reference frame. Both wing models were equipped with a six-degree-of-freedom ATI Mini-40 force balance that measured forces and moments at 1 kHz. Figure 3(b) shows an example of the postprocessing applied to the unfiltered lift signal. Each experiment was repeated five times and all measurements were ensemble averaged, as well as filtered at a cutoff frequency of 5 Hz to remove structural vibrations in the 8–10 Hz range.

Table I summarizes the experiments used in this study. All experiments were conducted at a geometric angle of attack of 0°. For the trapezoidal gust experiments, two different Reynolds numbers were tested at four gust ratios. The gust ratios were chosen to investigate two different regimes: a high gust ratio and a low gust ratio regime. The effective angles of attack seen by the wing when fully immersed in gusts of gust ratios 0.75 and 0.5 are 37° and 27°, respectively. The effective angles of attack seen by the wing when the gust ratios are 0.3 and 0.2 are 17° and 11°, respectively. The properties of the LEV are extracted from PIV using the vortex identification method proposed in Graftieaux *et al.* [45]. The Γ_1 criterion was used to identify the centroid of the leading edge vortex. The Γ_2 criterion was then used to identify the boundary of the vortex, and Stokes' theorem was used to compute the circulation using the vorticity within the identified boundary (see also the Supplemental Material [46] for the control volumes used in the integration).

The uncertainty of the PIV vector fields was quantified using a built-in DaVis error tool which uses correlation statistics to construct an error estimate [47]. The maximum uncertainty in the velocity field was 3.6% while the average error was about 1%. The paper also computes integral quantities of the vector field, such as vortex circulation. The error for these quantities was estimated by employing linear error propagation theory [48] to the numerical integration scheme used to

FIG. 4. The flowfield in Küssner's gust encounter model. The wing and wake are represented as vortex sheets and the local angle of attack of the airfoil changes according to the local gust velocity V.

compute these quantities. The average error was found to be approximately 8% of the instantaneous vortex circulation.

B. Küssner's gust-encounter model

Classical unsteady aerodynamics theory uses a set of simplifying assumptions to derive analytic or semi-analytic expressions for the loads on a wing section. Typically, the wing is modeled as a thin airfoil with a vortex sheet placed on its camber line. The wake is also modeled as a vortex sheet starting at the trailing edge and is assumed to be flat and frozen in the flow. Using the above simplifying assumptions along with the enforcement of no flow through the wing, as well as the Kutta condition and Kelvin's circulation theorem, load coefficients can be derived as a function of the unsteady operating conditions and wing kinematics. Using this approach, Wagner [5] successfully calculated the lift evolution of a wing due to a step change in its quasisteady bound circulation. Küssner [49] later used this result to calculate the load transients during a transverse gust encounter. He modeled the wing as a broken-line airfoil, whose local angle of attack and quasisteady bound circulation are computed from the gust velocity. The modeled flowfield is shown in Fig. 4. For a detailed derivation of Küssner's model the interested reader is pointed to Leishman [50, Chapter 8.1].

von Karman and Sears [51] decomposed the lift produced in this unsteady aerodynamics framework into three components: The quasisteady lift, the added-mass lift, and the lift due to the presence of the wake. The first component corresponds to the results of steady thin-airfoil theory, where wake vorticity is assumed to be infinitely far downstream of the wing. The second component corresponds to the vortex sheet that develops in order to enforce no flow through the wing during wing accelerations, and the last component corresponds to the vortex sheet that develops to counteract the downwash (or upwash) due to the wake. A paradox arises in the case of a gust encounter, as there is an added-mass force according to the definition of von Karman and Sears [51] but with no body accelerations. Corkery and Babinsky [52] showed that this force arises due to the change in the vortex sheet induced by the gust vorticity on the wing. In accordance with Kelvin's circulation theorem, all vorticity in the flow not shed by a body must sum to zero. Therefore, this induced vortex sheet must have no total circulation and is appropriately called "noncirculatory." It is worth noting that researchers have identified these vortex sheets even in the presence of flow separation and external vorticity [21,52,53]. In light of this evidence, in this work we assume that noncirculatory effects approximately superimpose with circulatory effects. The quasisteady lift and the lift due to the wake make up what is often called circulatory lift, as they are associated with the build-up of bound circulation. Further discussion on the resolution of this apparent paradox for the general case of a body immersed in a viscous flow can be found in Limacher *et al.* [54].

Each of the lift contributions are shown Fig. 5 for a trapezoidal gust profile with gust width of 1.4 chords and a sine-squared gust profile with a gust width of 2.6 chords. These forces have been obtained using unsteady vortex simulations which explicitly enforce the frozen wake and attached flow assumptions. Epps and Roesler [55] showed that this method accurately extracts the forces and circulations from classical unsteady theories, which often do not have closed-form time-domain solutions. These forces are extracted numerically from the vortex model in the following way: At

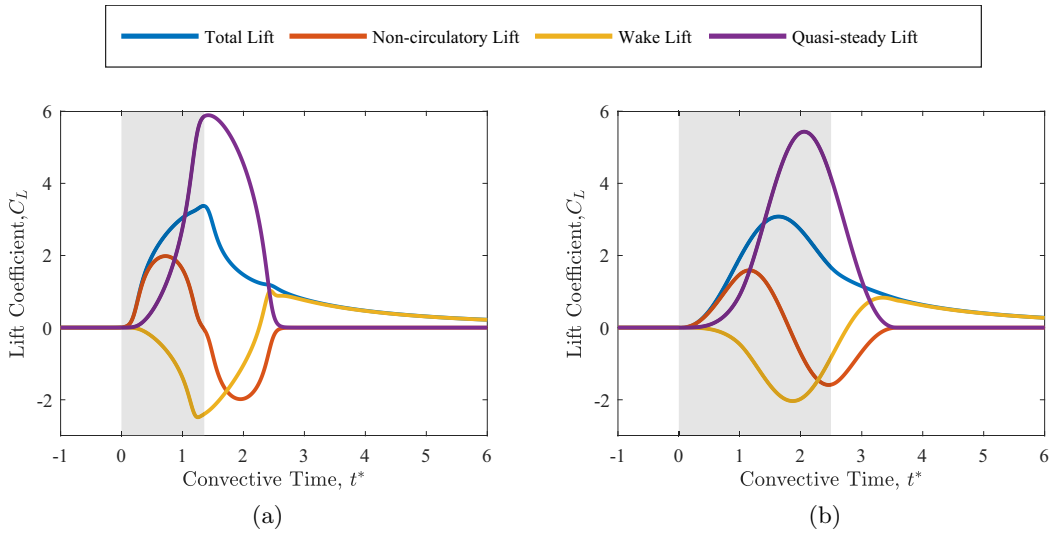

FIG. 5. Lift decomposition in Küssner's model for (a) trapezoidal gust profiles and (b) sine-squared gust profiles.

each time step, the bound vorticity distribution can be determined by solving the linear system $A\Gamma = \text{RHS}$, where A is a matrix containing the influence coefficients of the bound vortices, Γ is a vector containing the circulation of the bound vortices, and RHS is a vector containing the induced velocities from the flowfield. The circulatory and noncirculatory bound vorticity distributions are extracted by decomposing RHS into contributions from the shed vorticity and the gust, $RHS = RHS_{\text{gust}} + RHS_{\text{shed}}$, and then solving the two linear systems for Γ^{nc} and Γ^{c}. The corresponding circulatory and noncirculatory lift is then calculated using equation (2). The quasisteady lift L^{qs} is obtained by integration of the effective angle of attack induced by the gust along the chord of the wing. The lift induced by the wake, L^{w}, is calculated by subtracting the quasisteady lift from the total circulatory lift.

Figures 5(a) and 5(b) show that, during the early phases of the gust encounter, most of the force is noncirculatory. As the effective angle of attack increases, the quasisteady lift increases accordingly and there is a (delayed) build-up in bound circulation following Wagner's theory [5], which is balanced by opposite sign vorticity shed in the wake. This negative wake vorticity induces downwash on the wing and therefore has a negative contribution to the overall lift, as shown in Fig. 5. Similarly, as the effective angle of attack decreases in the later stages of the gust encounter, the quasisteady bound circulation also decreases. Consequently, the vorticity that is shed in the wake is positive and induces upwash on the wing and therefore has a positive contribution to lift. This positive wake-induced lift is the sole contributor to lift after the gust exits and persists for several chord lengths in accordance with Wagner's initial response.

C. Vortex-prediction methods

In this section we use vorticity flux methods to predict the general scaling between LEV growth and the relevant transverse gust encounter parameters. The goal can be stated as follows: Given some fixed geometry, what are the effects of the experimental parameters such as Reynolds number and gust ratio on the leading-edge vortex.

The problem at hand is depicted in Fig. 6. A control volume can be drawn around the LEV, shown in Fig. 6(a). The LEV circulation can be determined by integrating the fluxes on the boundary of the control volume. The LEV vorticity flux equation is derived in Ref. [16] and in two dimensions

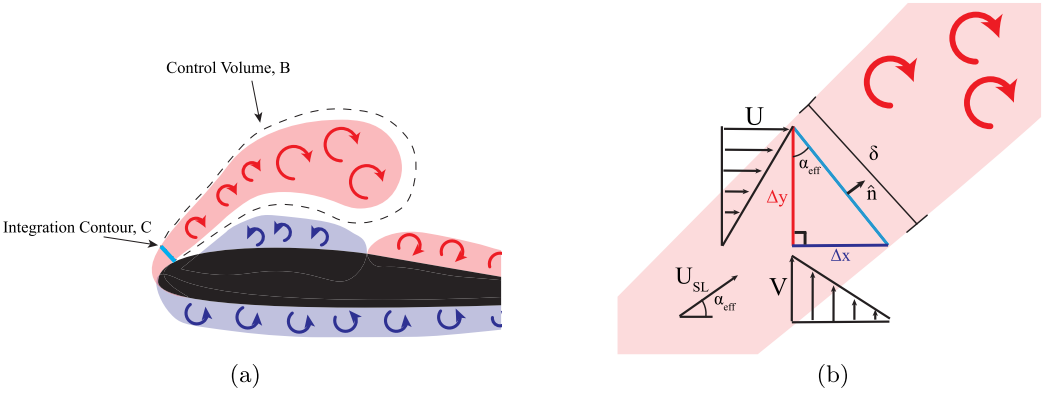

FIG. 6. (a) Control volume analysis of LEV growth and (b) geometry of the problem after simplifying assumptions have been applied.

it reads

$$\frac{\mathrm{d}\Gamma}{\mathrm{d}t} = \int_B \omega_z \boldsymbol{u} \cdot \hat{\boldsymbol{n}} \mathrm{d}B + \int_B \nu \frac{\mathrm{d}\omega_z}{\mathrm{d}\hat{n}} \mathrm{d}B, \tag{6}$$

where $\hat{\boldsymbol{n}}$ is the normal vector along B. The first term represents the convective flux and the second term represents the diffusive flux through the control volume boundary B. All of the vorticity of the LEV originates from the leading edge shear layer and therefore the integral in equation (6) is only nonzero along the part of the control volume boundary intersecting the shear layer C. Furthermore, as noted by Eldredge and Jones [16], the diffusive flux is likely to be small when compared with the convective flux through the shear layer. Therefore the integral can be simplified to

$$\frac{\mathrm{d}\Gamma}{\mathrm{d}t} = \int_C \omega_z \boldsymbol{u} \cdot \hat{\boldsymbol{n}} \mathrm{d}C. \tag{7}$$

The angle of curve C is fixed by the effective angle of attack seen at the leading edge, α_{eff}, shown in Fig. 6(b). Assuming a linear profile for the two velocity components across the shear layer, the vorticity can be written as the total velocity over the shear layer thickness,

$$\omega_z = \left(\frac{\mathrm{d}u}{\mathrm{d}y} - \frac{\mathrm{d}v}{\mathrm{d}x}\right) \approx \left(\frac{\sqrt{U_\infty^2 + V^2}}{\delta}\right),$$

where V is the local vertical velocity induced by the gust. The assumptions stated above and shown in Fig. 6(b) imply that the velocity vector in the integral in equation (7) is always normal to curve C, i.e., $\boldsymbol{u} \cdot \hat{\boldsymbol{n}} = (u^2 + v^2)^{1/2}$. Introducing a parametric variable $r \in [0, 1]$, equation (7) can be written and evaluated as shown below,

$$\begin{aligned}
\frac{\mathrm{d}\Gamma}{\mathrm{d}t} &= \int_C \omega_z \boldsymbol{u} \cdot \hat{\boldsymbol{n}} \mathrm{d}C \\
&\propto \int_0^1 \left(\frac{\sqrt{U_\infty^2 + V^2}}{\delta}\right) \sqrt{U_\infty^2 + V^2} r \delta \mathrm{d}r \\
&\propto \frac{1}{2} U_\infty^2 (GR^2 + 1).
\end{aligned} \tag{8}$$

The proportionality symbol has been used to emphasize that this is not an exact relationship because the flow acceleration effects around the leading edge have been ignored. For example, Fage and Johansen [56] found that for an airfoil at a high angle of attack, the velocity of the shear layer, U_{SL}, is

about 35%–50% higher than the freestream velocity, depending on the angle of attack. Furthermore, induced velocities by the bound vorticity and LEV will also change the shear layer velocity. This will inevitably lead to errors, but the elementary scaling effects of the experimental parameters can still be captured. An identical calculation can be carried out for the size of the LEV by integrating the mass flux across curve C.

$$\begin{aligned}\frac{\mathrm{d}A_{\mathrm{LEV}}}{\mathrm{d}t} &= \int_C \boldsymbol{u}\cdot\hat{\boldsymbol{n}}\mathrm{d}C \\ &\propto \int_0^1 \sqrt{U_\infty^2 + V^2}\, r\delta \mathrm{d}r \\ &\propto \frac{\delta}{2} U_\infty \sqrt{GR^2+1}. \end{aligned} \tag{9}$$

This calculation shows that the LEV area has a direct dependence on the shear layer thickness δ, a quantity not known *a priori*. Assuming that the vorticity in the shear layer originates at a stagnation point on the pressure side [57], and that the stagnation point flow is quasisteady since the angle of incidence in a trapezoidal gust is approximately constant, the Hiemenz equations [58] can be used to approximate the thickness of the shear layer, as discussed by Widmann and Tropea [38] and Schlichting and Gersten [59]. This approximation is given by

$$\delta = 2.4\sqrt{\frac{\nu}{a}}, \tag{10}$$

where ν is the kinematic viscosity of the fluid and a is a parameter that describes the local flow curvature around the stagnation point on the pressure side, i.e., $a = U_\infty(x, y)/x = -V(x, y)/y$, with the origin of the coordinate system located at the stagnation point. a is proportional to U_∞, $a = a_0 U_\infty$, and equation (10) can then be written as

$$\delta = 2.4\sqrt{\frac{\nu}{a_0 U_\infty}}. \tag{11}$$

Equation (11) can be used in conjunction with equation (9) to predict the area growth of an LEV. Unfortunately, for the trapezoidal gust experiments there was no optical access of the pressure side of the wing during the gust encounter and therefore a_0 cannot be directly computed. Instead, a steady vortex panel method was used to compute the location of the stagnation point and the parameter a_0. It is found to be 1.67 and 2.59 for gust ratios 0.75 and 0.5, respectively. This method was also used in Ref. [38] to calculate a_0.

III. RESULTS

A. Flow morphology and Reynolds number effects

This section presents the general flow evolution characteristics, as well a comparison between the experimental force transients and those predicted by Küssner's model. The effects of Reynolds number on the flow and loads are also briefly explored, as previous Reynolds number independence results have only been demonstrated for flat plate wings [60–62]. The low gust ratio regime consists of gust ratios 0.2 and 0.3 and the high gust ratio regime consists of gust ratios 0.5 and 0.75. Each gust ratio is repeated at a different Reynolds number as shown in Table I. For brevity, flowfields only for $GR = 0.3$ and $GR = 0.75$ are presented.

1. High gust ratio regime

Figure 7 depicts the gust encounter vorticity fields at four different time steps for $GR = 0.75$. $tU_\infty/c = 0$ corresponds to the leading edge entering the gust and $tU_\infty/c = 1.4$ corresponds to the leading edge exiting the gust. Figure 8 shows the LEV circulations and areas for the cases

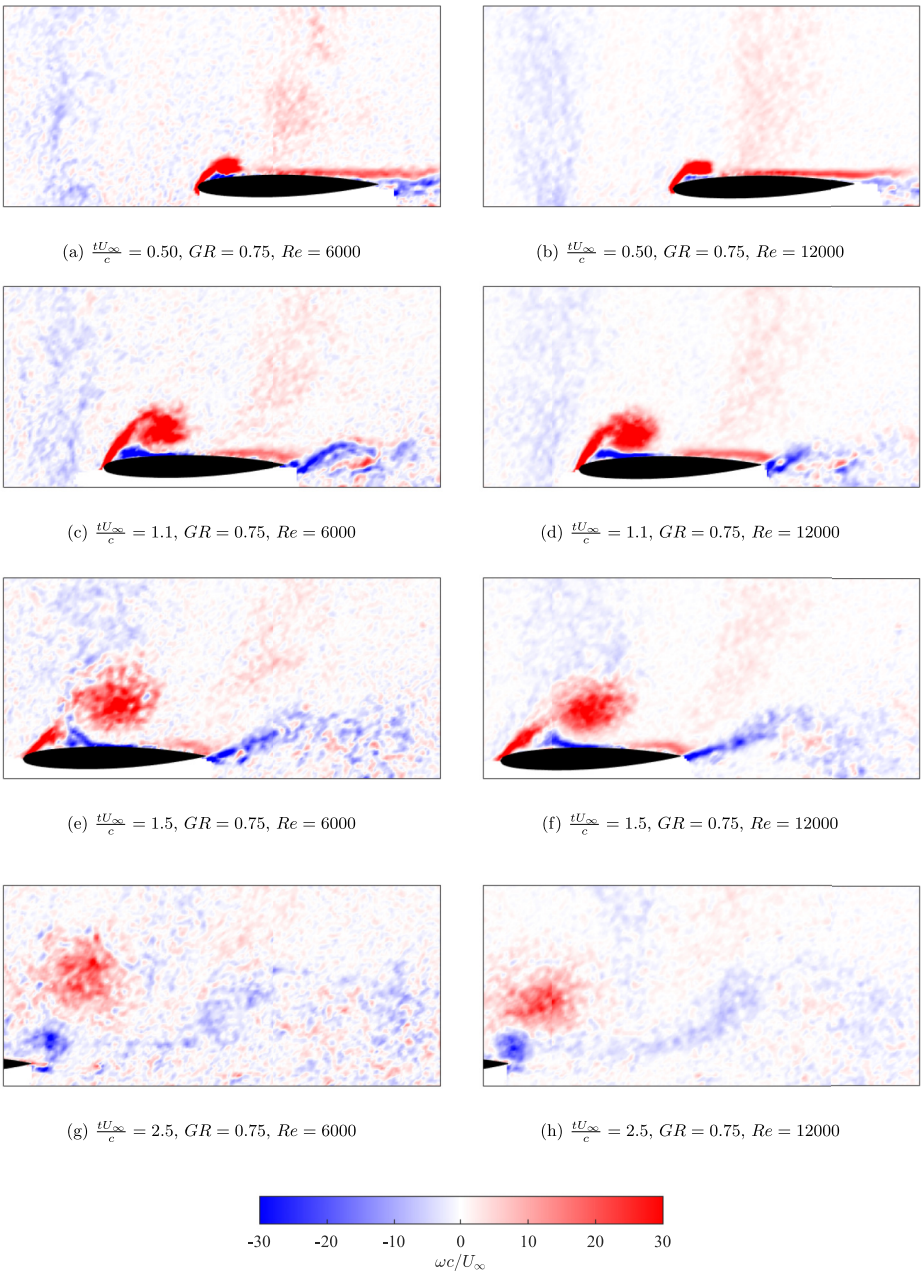

FIG. 7. The vorticity fields for $GR = 0.75$ at (left) Re = 6000 and (right) Re = 12 000.

$GR = 0.50$ and $GR = 0.75$ which have been extracted from PIV using the method discussed in Sec. II A. At $tU_\infty/c = 0.5$ the flow for both Reynolds numbers has already separated and formed a small but coherent LEV. The vortex has the same strength for both Reynolds numbers but for Re = 6000, the vortex encompasses a slightly larger area as shown in Fig. 8(b). For $tU_\infty/c = 1.1$, a large region of secondary vorticity has formed under the LEV and the flow is attached past the midchord. As the wing moves through the gust the primary and secondary vorticities grow in

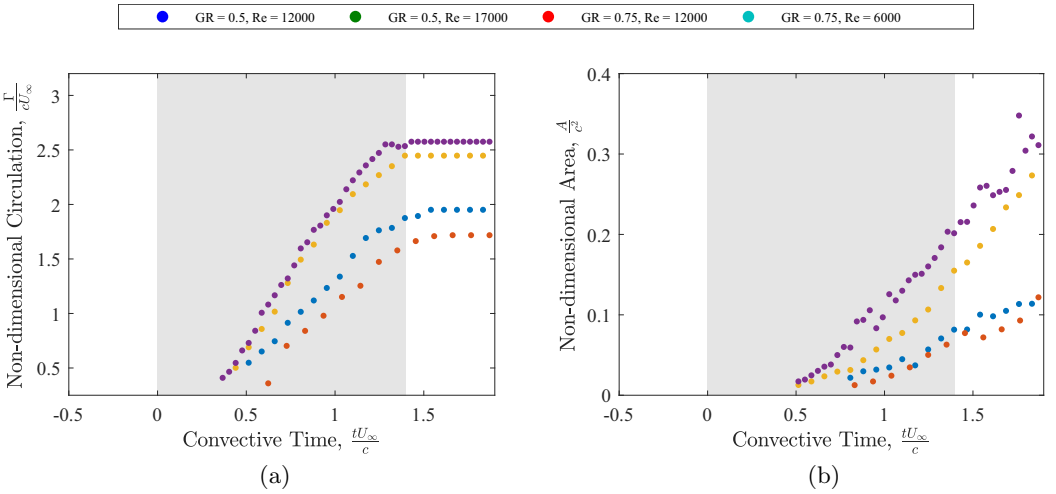

FIG. 8. The evolution of (a) the nondimensional circulation and (b) the nondimensional area of the LEV for the high-gust-ratio cases.

strength and the reattachment point moves down the chord of the wing. As the wing is exiting the gust at $tU_\infty/c = 1.5$, the LEV is noticeably larger for Re = 6000 as well as at a higher vertical position with respect to the wing. This is consistent with the fact that low Reynolds numbers promote viscous effects and the shear layer (originally a boundary layer on the leading edge with thickness $\propto \mathrm{Re}^{-0.5}$) has diffused over more fluid and therefore has more mass. Although at both Reynolds numbers the secondary vorticity is separating at $tU_\infty/c = 1.5$, the separation at Re = 6000 is more advanced and has partly severed the advection of vorticity into the LEV. This is again consistent with the fact that at lower Reynolds numbers secondary vorticity is more diffuse but also more susceptible to separation. Thus, for a given imposed adverse pressure gradient, the vortex-wall interaction is expected to be more advanced. Before the boundary layer eruption mechanism can fully detach the LEV, the wing exits the gust and the LEV is shed. As the wing moves past the LEV in Figs. 7(g) and 7(h), the reattachment point eventually reaches the trailing edge which induces flow reversal and a small trailing edge vortex (TEV) forms. A topological perspective on this flow reversal mechanism can be found in Rival *et al.* [41] for plunging kinematics. Furthermore, from Fig. 8 it is clear that the Reynolds number also affects the convective time of LEV onset, t^*_{onset}. As expected, increasing the Reynolds number delays the onset of flow separation and LEV formation.

2. Low gust ratio regime

The flowfields for $GR = 0.3$ are shown in Fig. 9. At $tU_\infty/c = 0.5$ the flow is fully attached. The flow develops differently for each Reynolds number as the wing moves through the gust at $tU_\infty/c = 1.1$. At Re = 28 000 a boundary layer instability is seen at this time on the surface of the airfoil, while at Re = 12 000 there is shear layer roll-up at the leading edge. At $tU_\infty/c = 1.5$ this leading-edge vortex has grown and is forcing flow reattachment, while at Re = 28 000 no such forcing mechanism exists and the flow is separating at the trailing edge.

3. Force measurements

Figure 10 depicts the lift coefficients for each of the gust encounters discussed in Secs. III A 2 and III A 1. For the low gust ratio cases ($GR = 0.2$, $GR = 0.3$) the force coefficients are larger when the Reynolds number is lower. This is consistent with the results seen in Sec. III A 2. At low gust ratios, the effective angle of attack is close to the static stall angle of attack, which is known to be a strong function of the Reynolds number. Therefore, changes in the Reynolds number can change

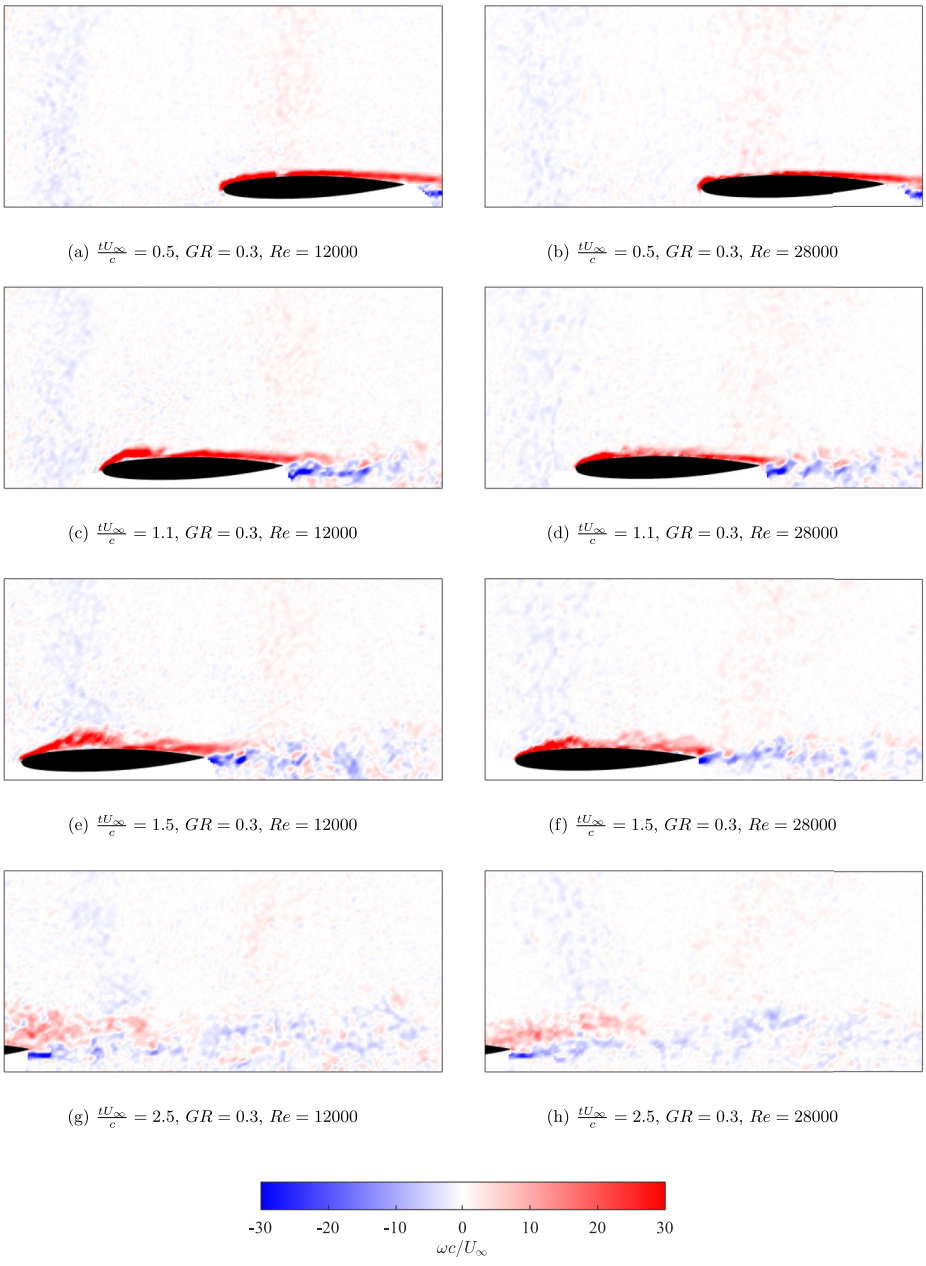

FIG. 9. The vorticity fields for $GR = 0.30$ at (left) Re = 12 000 and (right) Re = 28 000.

the separation dynamics of the encounter. As shown in Fig. 9, the flow separates at the leading edge at $GR = 0.3$, Re = 12 000 but not at $GR = 0.3$, Re = 28 000. Furthermore, this effect can be seen in the gust ratio normalized lift coefficients of Fig. 10(b). The high Reynolds number cases at low gust ratios converge to a smaller peak coefficient than the rest of the cases. A two sample t-test has been used to verify that the differences in maximum lift coefficient between Reynolds numbers is statistically significant at the 5% significance level.

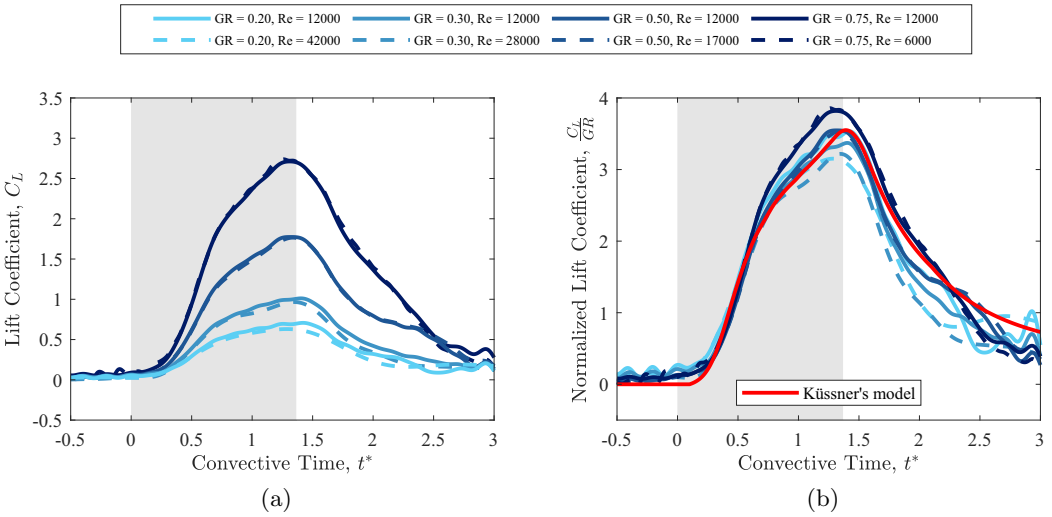

FIG. 10. Lift coefficient comparison for different gust ratios and Reynolds numbers for a blunt-edged airfoil encountering a trapezoidal gust: (a) non-normalized (b) normalized by gust ratio.

Given the similarity of the flowfields and the strengths of the LEVs, it is not surprising that in the high gust ratio regime lift is independent of Reynolds number. This can be attributed to the fact that at high gust ratios the boundary layer effectively separates at the leading edge, not allowing any Reynolds number dependent effects to materialize. It is worth noting that the difference in size of the LEV as shown in Fig. 8(b) does not affect the forces. However, this might not always hold true, as the size of the LEV can trigger different LEV detachment mechanisms [38] which can in turn change the dynamics of the LEV. Figure 10(b) shows that the well-known gust ratio scaling is appropriate for high gust ratio gust encounters with rounded leading-edge wings. Figure 10(b) also shows the lift response of Küssner's model for the trapezoidal gust shape. As observed in previous studies, the overall agreement with experimental data is good. The success and shortcomings of the model will be investigated in Sec. III C.

B. Leading-edge vortex growth

In this section the vortex integral properties discussed in Sec. II C are used to study the growth of the vorticity shed from the leading edge. A trapezoidal gust has an approximately uniform gust ratio across its width. Therefore, the LEV circulation in equation (8) and LEV size in equation (9), written in terms of the nondimensional variables scale as follows:

$$\frac{\Gamma}{cU_\infty} \propto \frac{1}{2}(GR^2+1)t^*, \tag{12}$$

$$\frac{A}{c^2} \propto 1.2t^*\sqrt{\frac{GR^2+1}{(a_0 c)\mathrm{Re}}}. \tag{13}$$

According to this formulation the growth of nondimensional circulation is linear in t^* with slope proportional to (GR^2+1). The growth of the nondimensional LEV size is also linear in t^* but with a slope that is governed by three nondimensional parameters: gust ratio, Reynolds number, and the product of chord with a_0, the streamline curvature around the stagnation point (for details on its calculation, see Sec. II C).

Equations (12) and (13) suggest an alternative scaling of the LEV growth. Figure 11 depicts the data of Fig. 8 normalized by the prediction of equations (12) and (13) for each case, i.e.,

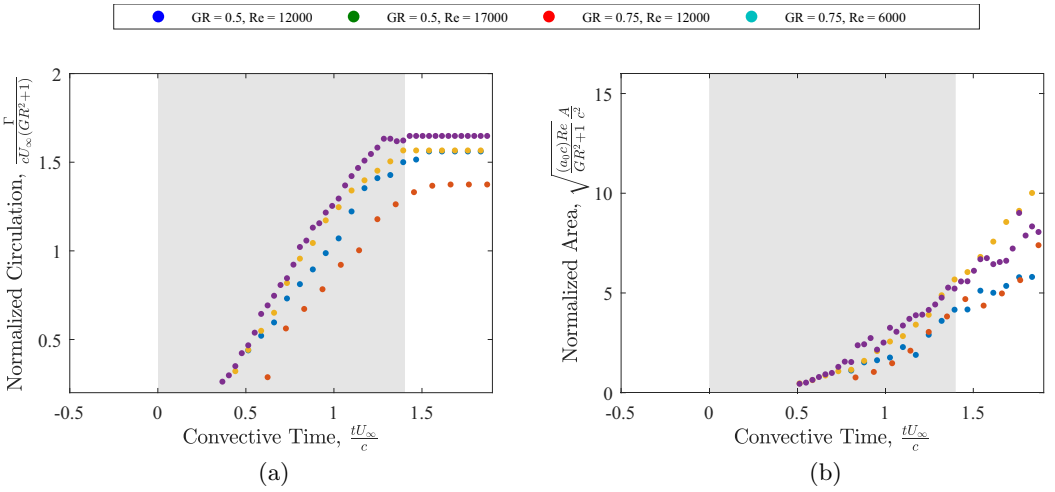

FIG. 11. Normalized LEV properties using the shear layer scaling suggested by equations (12) and (13): (a) normalized LEV circulation and (b) normalized LEV area.

$(GR^2 + 1)$ for the circulations, and $(GR^2 + 1)^{0.5}(a_0c)^{-0.5}\mathrm{Re}^{-0.5}$ for the areas. The normalized LEV properties in Fig. 11 have similar growth rates across the different cases, which suggests that, for the parameter space examined, the LEV circulation and size growth are approximately proportional to the quantities suggested by equations (12) and (13). The disparity in the growth rates increases with convective time. This could be attributed to the simplified calculation of the shear layer velocity. At the initial stages of the gust encounter, the flowfield is dominated by gust vorticity. However, in the latter stages, there is significant build up of bound and LEV circulation, which affect the shear layer velocity. The two cases with $\mathrm{Re} = 12\,000$ remain in fair agreement, while the case with $\mathrm{Re} = 6000$ has a slightly larger maximum LEV circulation, and the case with $\mathrm{Re} = 17\,000$ has a slightly lower maximum LEV circulation. This suggests that the Reynolds number is important in the leading edge vorticity production after the wing has spent more than one convective time inside the gust.

C. Comparison of experimental and theoretical circulations

This section evaluates the differences in circulation budget and lift between the experimental data and Küssner's model. The normalized experimental and theoretical lift coefficients for the two different gust profiles are presented in Fig. 12. The model performs remarkably well during the early phases of the gust encounter. This suggests that the experimental lift early in the gust encounter is indeed noncirculatory as shown in Fig. 5. This phenomenon has been investigated by Corkery and Babinsky [52] for wings with small thickness and extended to bodies of finite thickness by Gehlert and Babinsky [53]. Effects that do not scale with gust ratio appear around $t^* = 0.75$, approximately coincident with the onset of flow separation. Namely, the rate of increase of normalized lift slightly increases with increasing gust ratio, and the convective time of the peak lift coefficient slightly decreases with increasing gust ratio. This has also been reported by Andreu-Angulo *et al.* [30] and Andreu-Angulo and Babinsky [28] (see, for example, Fig. 18 in Andreu-Angulo and Babinsky [28]). After the peak lift coefficient is reached, the experimental lift has a sharper drop-off than Küssner's model. This drop-off is more pronounced for the sine-squared gust encounter.

To investigate the above results, the experimental circulations shed from the leading and trailing edges are quantified. The partitioning is carried out as shown in Fig. 13(a). All vorticity shed from the leading edge is counted as LEV circulation Γ_{LEV}, while all vorticity shed from the trailing edge is counted as wake circulation Γ_w. As the sum of gust circulation must be zero, the bound circulation Γ_b can be approximated by the (negative) sum of the leading- and trailing-edge circulations.

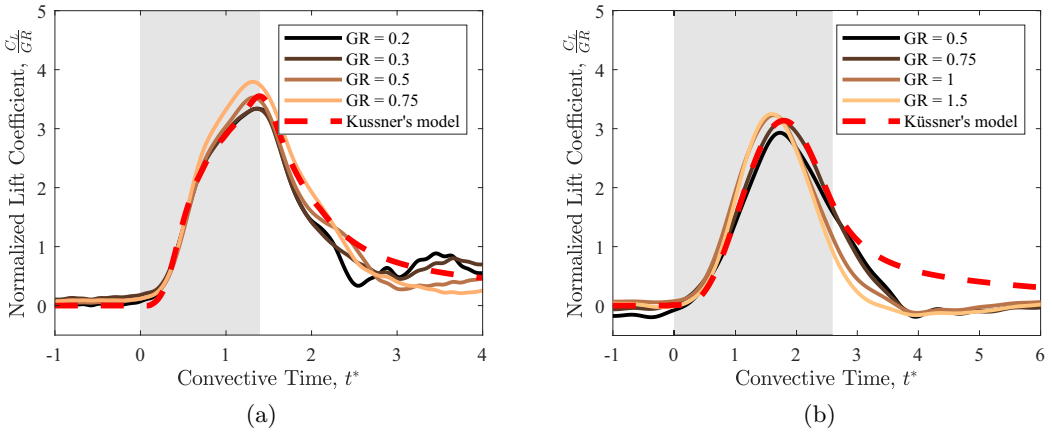

FIG. 12. Experimental and theoretical lift coefficients normalized by gust ratio for (a) trapezoidal gust profile and (b) sine-squared gust profile.

Therefore, $\Gamma_b = -(\Gamma_{\text{LEV}} + \Gamma_w)$. The leading edge circulation is captured by measuring the flux of vorticity through a control volume centered at the leading edge with side length 8% of the chord. The trailing edge circulation is quantified by measuring the flux of vorticity through a plane located at the trailing edge which is perpendicular to the wing. The flux surfaces used are shown in Fig. 13(b).

A similar circulation decomposition can be applied to Küssner's model. Since in this case the flow is attached, the bound circulation must be equal and opposite of the total circulation in the wake, $\Gamma_b^K = -\Gamma_w^K$, where $()^K$ denotes quantities related to Küssner's model. The bound circulation in Küssner's model can be further decomposed into quasisteady circulation Γ_{qs}^K and the circulation due to the image vorticity of the wake, Γ_{IW}^K.

Figure 14 depicts the evolution of each circulation in Küssner's model as well as the experimental circulations for sine-squared gust encounters at gust ratios of 0.75 and 1. From Fig. 12(b), $GR = 0.75$ shows the best agreement with Küssner's model. The circulation trends for this case are shown in Fig. 14(a). Early on in the gust encounter, both experimental and theoretical circulations are small. This is consistent with the understanding that in this phase of the gust encounter most

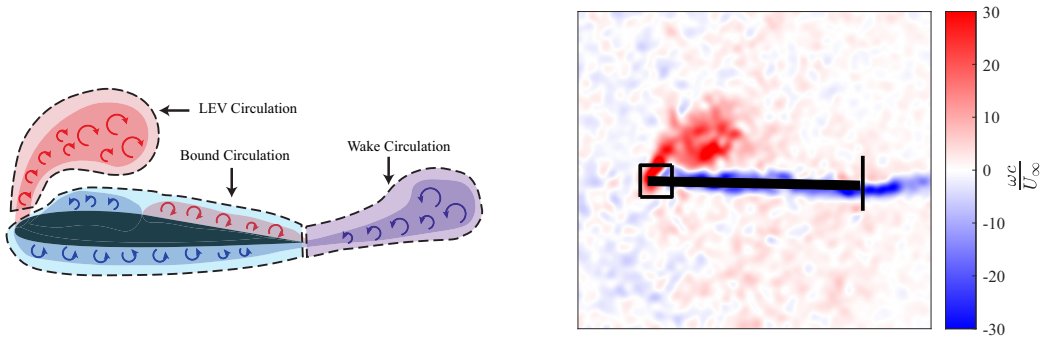

FIG. 13. The circulation of the LEV was measured from the flux of positive vorticity through a square control volume centered at the leading edge. Circulation shed in the wake was measured from the flux of total circulation through a plane perpendicular to the trailing edge. (a) Decomposition of the circulation in the flowfield and (b) surfaces through which vorticity fluxes were measured.

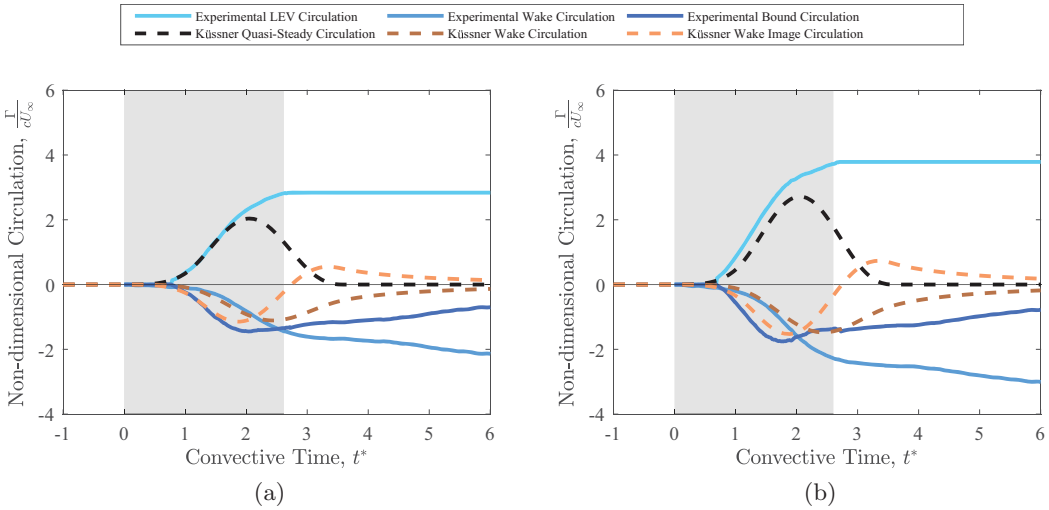

FIG. 14. Experimental and theoretical circulation trends during a transverse gust encounter for a sine-squared gust at (a) $GR = 0.75$ and (b) $GR = 1$.

of the force is noncirculatory as discussed in Sec. II B and shown in Fig. 5. As the effective angle of attack increases, the flow separates and a LEV forms at a convective time of $t^* = 0.75$. As positive circulation accumulates in the LEV, negative bound circulation develops on the wing which is manifested in the wing's attached pressure side boundary layer, as well as suction side secondary vorticity. Circulation shed from the trailing edge starts to increase as the wing is fully immersed in the gust at around $t^* = 1$. Interestingly, this trailing edge circulation very nearly follows the theoretical circulation shed in Küssner's model up until $t^* = 2$. Since in Küssner's model $\Gamma_w^K = -\Gamma_b^K$ and in the experiments $\Gamma_w = -(\Gamma_{\mathrm{LEV}} + \Gamma_b)$, it then follows that $\Gamma_{\mathrm{LEV}} + \Gamma_b = \Gamma_b^K$, i.e., although the real viscous flow is separated, the bound circulation of Küssner's inviscid model captures the combined circulations of the bound vortex and LEV in the experiments.

For $GR = 0.75$, the circulation trends possess two more interesting characteristics: (i) The LEV circulation is approximately equal to the theoretical quasisteady circulation and (ii) the experimental bound circulation is approximately equal to the theoretical bound circulation induced by the wake in Küssner's model (the image vorticity required to enforce no flow through the wing, and the Kutta condition). In other words, Küssner's bound circulation approximates the experimental bound vortex-LEV pair with the LEV carrying positive circulation instead of the quasisteady bound vortex. This fact, along with favorable vortex dynamics (to be discussed in Sec. III D), gives the model predictive power over a significant portion of the gust encounter.

However, this phenomenon breaks down at around $t^* = 2$, at which point the circulations diverge between theory and experiment. This is caused by the following discrepancy between Küssner's model and the real separated flow: In the attached flow theoretical model, the wing's quasisteady circulation decreases as it nears the exit of the gust and positive upwash-inducing vorticity must be shed to satisfy Kelvin's circulation theorem, as discussed in Sec. II B. This is shown in Fig. 15(a), where in the second half the gust encounter the circulation shed from the trailing edge is positive. In contrast, in the real separated flow it is the LEV that is supplying the lift and not the bound circulation. As the effective angle of attack decreases, the wing will shed part of its bound circulation, which in this case is negative and downwash-inducing. This is depicted in Fig. 15(b) and can be seen in the PIV vorticity fields of Figs. 7(e) and 7(f). The absence of upwash-inducing wake vorticity is the reason a much sharper drop-off is observed in experiments when compared with Küssner's model. The model is only able to capture the correct wake topology while the quasisteady circulation is increasing. This is also shown quantitatively in Fig. 14, where in the second half of

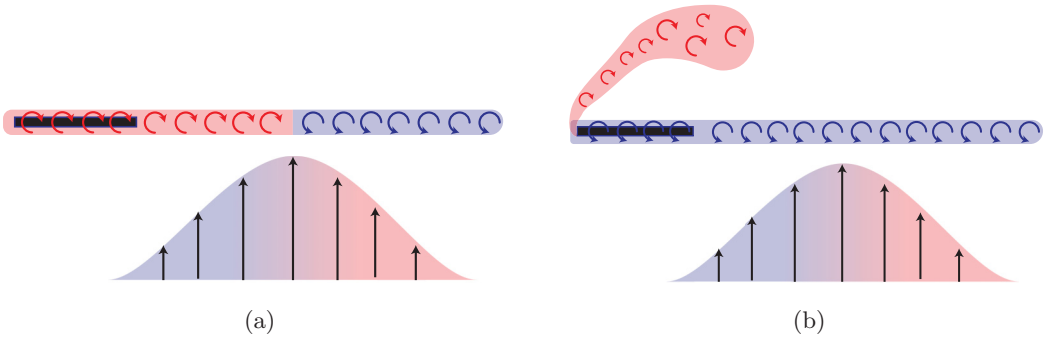

FIG. 15. Wake vortex sheet distributions during a transverse gust encounter for (a) Küssner's model and (b) experiments.

the gust encounter the experimental wake circulation continues to decrease, while Küssner's wake circulation increases until it reaches zero. This persistent negative circulation in the experimental wake and the negative bound circulation after the gust exit often cause negative lift in the aftermath of the encounter (see for example, Figs. 12(b) and 18 in Ref. [28]). Upon gust exit the effective angle of attack is zero. The LEV is shed and is no longer supplying much positive lift, but the wake is still inducing downwash, thus causing negative lift.

Further discrepancy between theory and experiments can be caused by the fundamental difference in the vorticity generation mechanism between linear theory and separated lifting flows. The circulation of Küssner's quasisteady bound vortex is created from the integrated effect of the effective angle of attack over the chord of the wing and thus scales linearly with gust ratio. In contrast, the LEV has no such restriction. In Sec. III B it was shown that, under certain conditions, the vorticity generated at the leading edge can instead be a function of the gust ratio squared, and only a function of the effective angle of attack at the leading edge. Furthermore, it has been observed in this study as well as in studies of wings with unsteady kinematics [39,63], that increasing the magnitude of the unsteady parameters can lead to earlier flow separation and thus a decreasing time of LEV onset, t^*_{onset}. This can be seen in Fig. 14(b) which shows the circulation trends for Küssner's model and the experiments at a gust ratio of one. In this case, the LEV circulation leads the quasisteady circulation in Küssner's model by approximately 0.1 convective times. The corresponding lift transient in Fig. 12(b) shows similar characteristics, as the peak lift coefficient is earlier than Küssner's model and the rate of increase of lift is slightly larger for higher gust ratios. This effect can also be seen in Fig. 12(a) for a trapezoidal gust, where again the rate of increase of normalized lift increases with gust ratio. It is worth noting that the rate of increase of LEV vorticity does not directly translate to a corresponding increase in lift, as the bound circulation also needs to be accounted for. Unfortunately, bound circulation is a function of the proximity of the LEV to the wing, as well as the size of the region the LEV occupies, and thus its growth rate is a nontrivial function of gust ratio. The data suggest that the circulatory lift during a transverse gust encounter increases with a factor slightly larger than gust ratio, i.e., GR^n where $1 < n < 2$.

D. Vortex detachment

In the previous section it was observed that, early in the gust encounter, Küssner's model captures the general circulatory characteristics of the real viscous flow. However, equation (2) implies that the convection of vorticity is also a contributor to the overall lift of the system. Indeed, the experimental agreement with Küssner's model demonstrated in this study and in previous studies [25–27] is expected to break down after some critical gust width, due to the convection of the LEV. For long enough gusts, the LEV will reach its maximum circulation and detach. The purpose of this section is to quantify the critical gust width and to show that the gust widths under investigation are shorter

than the critical vortex formation timescale. Thus, we can expect the LEV to remain attached for the duration of gust encounter. In this study, an LEV is called attached if it is connected to the feeding shear layer while also convecting at a speed close to the freestream velocity.

Stall delay has been shown to be a function of the unsteady flow parameters [63]. Le Fouest *et al.* [65] quantified the stall delay for pitching wings as a function of reduced pitch rate. They found that the delay obeys a decaying power law, and, as pitch rate increases, the delay asymptotically approaches the vortex formation number discussed in Sec. I, i.e., the maximum time the LEV can grow before reaching its maximum circulation and detaching. For a gust encounter, the pitch rate corresponds to the rate of change of the effective angle of attack. This means that the high-amplitude, high-frequency gust encounters presently being studied have an effective pitch rate that is an order of magnitude higher than that required to achieve vortex formation stall delay. Therefore, it is expected that the vortex formation timescale is the limiting timescale of the observed lift transient and can be used to approximate how wide a gust needs to be for stall to occur—stall in this case referring to the lift drop-off at the end of the dynamic stall process.

Starting from the definition of vortex formation time $\hat{T} = C\Gamma/(D\Delta U)$ for leading-edge vorticity production, the constant C is often taken to be one, as discussed by Rival *et al.* [41], and the characteristic length-scale D to be the chord. Furthermore, the velocity across the shear layer during a gust encounter is $U_{SL} = (U_\infty^2 + V^2)^{1/2} = U_\infty(GR^2 + 1)^{1/2}$ and the circulation of the LEV is expected to scale with U_{SL}^2 [38,40,66], i.e., $\Gamma_{\text{LEV}} = KU_{SL}^2 t$, where K is the proportionality constant between the square shear layer velocity and the LEV circulation. Thus, we have the following:

$$\hat{T} = \frac{C\Gamma_{\text{LEV}}}{c\Delta U} = \frac{KtU_{SL}^2}{cU_{SL}} = K\frac{U_\infty t}{c}\sqrt{GR^2+1} = Kt^*\sqrt{GR^2+1}. \tag{14}$$

According to vortex formation theory, there a exists a critical formation time $\hat{T}_{\text{crit}}$ at which the LEV will reject any additional vorticity and detach. Using the above relation it is then possible to recover the critical convective time (or the gust width-to-chord ratio) that a wing can spend inside a gust without stalling. Rearranging equation (14) gives

$$t^*_{\text{crit}} = \left(\frac{w}{c}\right)_{\text{crit}} = \frac{\hat{T}_{\text{crit}}}{K\sqrt{GR^2+1}}. \tag{15}$$

Equation (15) states that as the gust ratio increases, the critical width-to-chord ratio decreases since the LEV will reach its critical circulation faster. To the authors knowledge, there exist no experimental apparatus that can vary the gust width to determine the constants in equation (15). Badrya *et al.* [64] conducted a CFD study for sine-squared gusts, keeping the gust ratio fixed and varying the gust width. The lift coefficients are shown in Fig. 16 along with Küssner's prediction for each. Their results show that, for $GR = 0.8$, Küssner's theory captures the lift transient all the way up to a gust width-to-chord ratio of four, after which stall onset hampers the model's performance.

The experiments presented in this paper have a maximum gust width-to-chord ratio of 2.6, well below the critical width-to-chord ratio predicted above, even after accounting for a higher gust ratio. Therefore, the LEV grows until the wing exits the gust at which point it detaches. This is evident in Fig. 8(a), as the peak circulation for each of the cases takes place as the wing is exiting the gust. Furthermore, Fig. 16 shows that for gust widths longer than four chords, the peak lift coefficient takes place before the wing starts exiting the gust. The detachment of the LEV is facilitated by a forced interaction between the primary shear layer and the secondary vorticity. The progression of the forced detachment is depicted in Fig. 17 for $GR = 0.75$, $\text{Re} = 12\,000$. In Fig. 17(a), the wing is fully immersed in the gust. The LEV is attached and the separation angle at the leading edge is high due to the high effective angle of attack. As the wing is exiting the gust in Figs. 17(b) and 17(c), the effective angle of attack gradually decreases and the shear layer moves closer to the wing surface where it interacts with the secondary vorticity. The downward-moving fluid of the secondary vorticity reverses part of the flow of the primary shear layer, reducing the advection of vorticity into

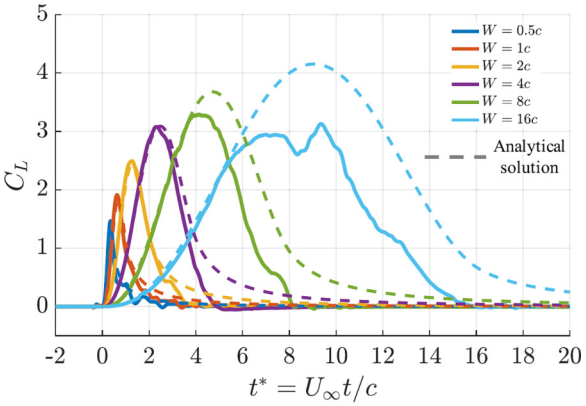

FIG. 16. Computational and theoretical lift transients for a sine-squared gusts, varying the gust width at a gust ratio of 0.8 [64].

the LEV. By $tU_\infty/c = 1.8$ in Fig. 17(d), the advection of vorticity into the vortex has ceased and the LEV has detached.

IV. CONCLUSION

The results show that Küssner's model provides a good first-order approximation of the lift transient experienced by wings with blunt leading edges during the initial stages of a transverse gust encounter. It is also observed that at low gust ratios ($GR = 0.2$ and $GR = 0.3$), wings with blunt leading edges experience increasing lift coefficients with decreasing Reynolds number. In contrast, at high gust ratios ($GR = 0.5$ and $GR = 0.75$), the lift transient experienced by blunt leading-edged wings is found to be independent of the Reynolds number.

The following concepts are applied to transverse gust encounters: (i) The notion of optimal vortex formation time, and (ii) LEV growth prediction through the integration of shear layer fluxes. The timescale of optimal vortex formation is shown to be larger than the timescale of the gust encounters studied in this paper. Thus, the LEV remains attached to the wing for the duration of the encounter and only detaches upon the wing's exit of the gust due to the rapid reduction of the effective angle of attack. The LEV flux model predicts that while the LEV is attached to the feeding shear layer, its circulation growth is proportional to $GR^2 + 1$ and area growth is proportional to $(GR^2 + 1)^{0.5}(a_0 c)^{-0.5}\mathrm{Re}^{-0.5}$. For the gust ratios and Reynolds numbers examined in this paper, fair agreement is seen between experiments and the flux model's predictions. The agreement deteriorates with increasing convective time. This could be attributed to the simplified calculation of the shear layer velocity made in the model, which only accounts for the gust vorticity. As the bound and LEV circulations become significant, they inevitably affect the shear layer velocity.

Comparison of the circulation shed in the wake of Küssner's model with the circulation shed in the wake during experiments leads to the following conclusion: Although the real viscous flow is separated, the bound circulation in Küssner's inviscid model captures the combined circulation of the bound vortex-LEV pair of the experiments, conditioned on an increasing quasisteady circulation. This result, along with the fact that the vortex remains attached for the duration of the gust encounter, indicates that Küssner's model captures the vertical impulse of the separated flow. In other words, if the LEV is attached, its circulation can be incorporated as part of the bound circulation of the inviscid model, resulting in an accurate model for the lift during transverse gust encounters.

The performance of Küssner's model deteriorates once the quasisteady circulation starts to decrease. This is because the lift-producing mechanisms between theory and experiment are fundamentally different, even though they produce similar values of lift while the quasisteady circulation

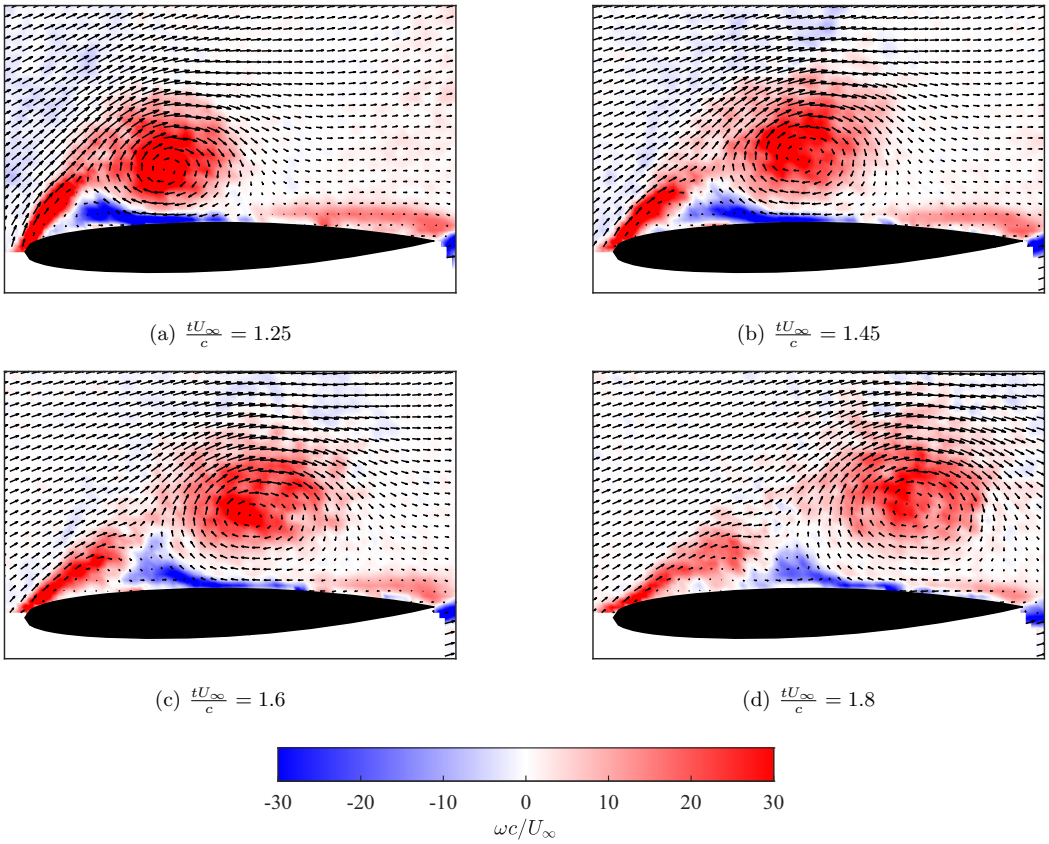

FIG. 17. Vorticity contours and velocity vector field in the reference frame of the wing at $GR = 0.75$ and $\mathrm{Re} = 12\,000$, depicting the progression of the forced LEV detachment upon gust exit.

is increasing. In the attached flow theoretical model, the positive circulation supplying the lift to the system is bound to the wing. In the real separated flow, the positive circulation supplying the lift is already shed and free to convect with the flow, while the bound circulation is in fact negative. Thus, when the quasisteady circulation decreases in the model, the circulation shed into the wake from the trailing edge is positive and upwash inducing, while in the experiments it is negative and downwash inducing. The absence of upwash-inducing wake vorticity is the reason a much sharper lift drop-off is observed in experiments. In other words, the lift drop-off in the model is governed by delayed response to a (negative) change in its quasisteady circulation, while in the experiments it is governed by the detachment of the LEV and the persistent shedding of negative circulation into the wake.

The above discussion presents a fundamental limitation on lift modeling using unsteady potential flow. While potential flows might be able to capture the general circulatory characteristics of separated lifting flows, they can only do so while the quasisteady circulation is increasing. Once the quasisteady circulation starts to decrease, the wake distribution will be of the wrong sign and the overall flow topology will be different. To improve lift prediction during the exit of the gust, the effect of the LEV on the bound circulation must be modeled. This can be done using a numerical vortex model that heuristically incorporates leading-edge separation.

Further discrepancies between the unsteady potential flow model and experiments are observed during the rise of the circulatory lift. This is attributed to the fact the bound vortex-LEV pair is not restricted to scale with gust ratio, as is the bound vortex in Küssner's model. In fact, the flux model

presented in Sec. III B shows that it is possible for the LEV growth to scale with the square of gust ratio. Furthermore, increasing the gust ratio decreases the time to LEV onset, t^*_{onset}, thus allowing circulatory effects to commence earlier. The culmination of these two effects cause the normalized lift peak coefficient to be earlier and higher with increasing gust ratio.

ACKNOWLEDGMENTS

The authors would like to thank P. Kirk and Dr. F. Lagor for the valuable discussions and their assistance with the design of the experiments. The authors would also like to thank Dr. H. Biler for obtaining the sine-squared gust encounter data. This material is based upon work supported by the National Science Foundation Award No. 2003951.

[1] R. T. Jones, *Classical Aerodynamic Theory*, 1050 (National Aeronautics and Space Administration, 1979).
[2] L. Prandtl, Über flussigkeitsbewegung bei sehr kleiner reibung, Verhandl. III, Internat. Math.-Kong., Heidelberg, Teubner, Leipzig, 1904, 484 (1904).
[3] J. Katz and A. Plotkin, *Low-Speed Aerodynamics* (Cambridge University Press, Cambridge, UK, 2001), Vol. 13.
[4] T. Theodorsen, General Theory of Aerodynamic Instability and the Mechanism of Flutter, Tech. Rep. (1949).
[5] H. Wagner, Über die entstehung des dynamischen auftriebes von tragflügeln (1924).
[6] P. Walker, Growth of circulation about a wing and an apparatus for measuring fluid motion, ARC report (1931).
[7] F. Manar and A. R. Jones, Evaluation of potential flow models for unsteady separated flow with respect to experimental data, Phys. Rev. Fluids **4**, 034702 (2019).
[8] P. Mancini, A. Medina, and A. R. Jones, Experimental and analytical investigation into lift prediction on large trailing edge flaps, Phys. Fluids **31**, 013106 (2019).
[9] H. Babinsky, R. J. Stevens, A. R. Jones, L. P. Bernal, and M. V. Ol, Low order modelling of lift forces for unsteady pitching and surging wings, in *54th AIAA Aerospace Sciences Meeting* (AIAA, Reston, VA, 2016), p. 0290.
[10] C. P. Ford and H. Babinsky, Lift and the leading-edge vortex, J. Fluid Mech. **720**, 280 (2013).
[11] M. V. Ol, L. Bernal, C.-K. Kang, and W. Shyy, Shallow and deep dynamic stall for flapping low Reynolds number airfoils, in *Animal Locomotion* (Springer, 2010), pp. 321–339.
[12] C.-k. Kang, Y. Baik, L. Bernal, M. Ol, and W. Shyy, Fluid dynamics of pitching and plunging airfoils of Reynolds number between 1×10^4 and 6×10^4, in *47th AIAA Aerospace Sciences Meeting Including the New Horizons Forum and Aerospace Exposition* (AIAA, Reston, VA, 2009), p. 536.
[13] K. Mulleners and M. Raffel, The onset of dynamic stall revisited, Exp. Fluids **52**, 779 (2012).
[14] W. J. McCroskey, Unsteady airfoils, Annu. Rev. Fluid Mech. **14**, 285 (1982).
[15] C. P. Ellington, The aerodynamics of flapping animal flight, Am. Zool. **24**, 95 (1984).
[16] J. D. Eldredge and A. R. Jones, Leading-edge vortices: Mechanics and modeling, Annu. Rev. Fluid Mech. **51**, 75 (2019).
[17] P. G. Saffman, *Vortex Dynamics* (Cambridge University Press, 1995).
[18] J. C. Wu, Theory for aerodynamic force and moment in viscous flows, AIAA J. **19**, 432 (1981).
[19] P. Gehlert and H. Babinsky, Linking the unsteady force generation to vorticity for a translating and rotating cylinder, in *AIAA Scitech 2019 Forum* (2019), p. 0347.
[20] P. Gehlert and H. Babinsky, Boundary layer vortex sheet evolution around an accelerating and rotating cylinder, J. Fluid Mech. **915**, A50 (2021).
[21] S. Corkery, H. Babinsky, and W. Graham, Quantification of added-mass effects using particle image velocimetry data for a translating and rotating flat plate, J. Fluid Mech. **870**, 492 (2019).

[22] D. T. Polet, D. E. Rival, and G. D. Weymouth, Unsteady dynamics of rapid perching manoeuvres, J. Fluid Mech. **767**, 323 (2015).
[23] S. Ōtomo, S. Henne, K. Mulleners, K. Ramesh, and I. M. Viola, Unsteady lift on a high-amplitude pitching aerofoil, Exp. Fluids **62**, 6 (2021).
[24] P. Stevens and H. Babinsky, Experiments to investigate lift production mechanisms on pitching flat plates, Exp. Fluids **58**, 7 (2017).
[25] H. Biler, C. Badrya, and A. R. Jones, Experimental and computational investigation of transverse gust encounters, AIAA J. **57**, 4608 (2019).
[26] C. Badrya, A. R. Jones, and J. D. Baeder, Unsteady aerodynamic response of a flat plate encountering large-amplitude sharp-edged gust, AIAA J. **60**, 1549 (2022).
[27] S. Corkery, H. Babinsky, and J. Harvey, On the development and early observations from a towing tank-based transverse wing–gust encounter test rig, Exp. Fluids **59**, 135 (2018).
[28] I. Andreu-Angulo and H. Babinsky, Mitigation of airfoil gust loads through pitch, AIAA J. **60**, 1 (2022).
[29] G. Sedky, A. Gementzopoulos, I. Andreu-Angulo, F. D. Lagor, and A. R. Jones, Physics of gust response mitigation in open-loop pitching manoeuvres, J. Fluid Mech. **944**, A38 (2022).
[30] I. Andreu-Angulo, H. Babinsky, H. Biler, G. Sedky, and A. R. Jones, Effect of transverse gust velocity profiles, AIAA J. **58**, 5123 (2020).
[31] G. Sedky, A. R. Jones, and F. D. Lagor, Lift regulation during transverse gust encounters using a modified Goman–Khrabrov model, AIAA J. **58**, 3788 (2020).
[32] B. Herrmann, S. L. Brunton, J. E. Pohl, and R. Semaan, Gust mitigation through closed-loop control. II. Feedforward and feedback control, Phys. Rev. Fluids **7**, 024706 (2022).
[33] S. J. Corkery and H. Babinsky, Force production mechanisms for a flat plate wing at low Reynolds numbers, in *2018 AIAA Aerospace Sciences Meeting* (AIAA, Reston, VA, 2018), p. 0816.
[34] M. Gharib, E. Rambod, and K. Shariff, A universal time scale for vortex ring formation, J. Fluid Mech. **360**, 121 (1998).
[35] J. O. Dabiri, Optimal vortex formation as a unifying principle in biological propulsion, Annu. Rev. Fluid Mech. **41**, 17 (2009).
[36] D. Rival, R. Manejev, and C. Tropea, Measurement of parallel blade–vortex interaction at low Reynolds numbers, Exp. Fluids **49**, 89 (2010).
[37] Y. S. Baik, L. P. Bernal, K. Granlund, and M. V. Ol, Unsteady force generation and vortex dynamics of pitching and plunging aerofoils, J. Fluid Mech. **709**, 37 (2012).
[38] A. Widmann and C. Tropea, Parameters influencing vortex growth and detachment on unsteady aerodynamic profiles, J. Fluid Mech. **773**, 432 (2015).
[39] J. Kissing, J. Kriegseis, Z. Li, L. Feng, J. Hussong, and C. Tropea, Insights into leading edge vortex formation and detachment on a pitching and plunging flat plate, Exp. Fluids **61**, 208 (2020).
[40] N. Didden, On the formation of vortex rings: Rolling-up and production of circulation, Z. Angew. Math. Phys. **30**, 101 (1979).
[41] D. E. Rival, J. Kriegseis, P. Schaub, A. Widmann, and C. Tropea, Characteristic length scales for vortex detachment on plunging profiles with varying leading-edge geometry, Exp. Fluids **55**, 1660 (2014).
[42] P. Sattari, D. E. Rival, R. J. Martinuzzi, and C. Tropea, Growth and separation of a start-up vortex from a two-dimensional shear layer, Phys. Fluids **24**, 107102 (2012).
[43] G. Sedky, H. Biler, and A. R. Jones, Experimental comparison of a sinusoidal and trapezoidal transverse gust, AIAA J. **60**, 3347 (2022).
[44] H. Biler, G. Sedky, A. R. Jones, M. Saritas, and O. Cetiner, Experimental investigation of transverse and vortex gust encounters at low Reynolds numbers, AIAA J. **59**, 786 (2021).
[45] L. Graftieaux, M. Michard, and N. Grosjean, Combining PIV, POD and vortex identification algorithms for the study of unsteady turbulent swirling flows, Meas. Sci. Technol. **12**, 1422 (2001).
[46] See Supplemental Material at http://link.aps.org/supplemental/10.1103/PhysRevFluids.9.014701 for the control volumes used to calculate the LEV properties in Fig. 8.
[47] B. Wieneke, PIV uncertainty quantification from correlation statistics, Meas. Sci. Technol. **26**, 074002 (2015).
[48] A. Sciacchitano and B. Wieneke, PIV uncertainty propagation, Meas. Sci. Technol. **27**, 084006 (2016).

[49] H. G. Küssner, Zusammenfassender bericht über den instationären auftrieb von flügeln, Luftfahrtforschung **13**, 410 (1936).
[50] G. J. Leishman, *Principles of Helicopter Aerodynamics* (Cambridge University Press, 2006).
[51] T. H. von Karman and W. R. Sears, Airfoil theory for non-uniform motion, J. Aeronaut. Sci. **5**, 379 (1938).
[52] S. J. Corkery and H. Babinsky, An investigation into gust shear layer vorticity and the added mass force for a transverse wing-gust encounter, in *AIAA Scitech 2019 Forum* (AIAA, Reston, VA, 2019), p. 1145.
[53] P. Gehlert and H. Babinsky, Noncirculatory force on a finite thickness body encountering a gust, AIAA J. **59**, 719 (2021).
[54] E. Limacher, C. Morton, and D. Wood, Generalized derivation of the added-mass and circulatory forces for viscous flows, Phys. Rev. Fluids **3**, 014701 (2018).
[55] B. P. Epps and B. T. Roesler, Vortex sheet strength in the sears, Küssner, Theodorsen, and Wagner aerodynamics problems, AIAA J. **56**, 889 (2018).
[56] A. Fage and F. Johansen, On the flow of air behind an inclined flat plate of infinite span, Proc. R. Soc. London, Ser. A **116**, 170 (1927).
[57] B. R. Morton, The generation and decay of vorticity, Geophys. Astrophys. Fluid Dyn. **28**, 277 (1984).
[58] K. Hiemenz, Die grenzschicht an einem in den gleichformigen flussigkeitsstrom eingetauchten geraden kreiszylinder, Dinglers Polytech. J. **326**, 321 (1911).
[59] H. Schlichting and K. Gersten, *Boundary-Layer Theory* (Springer Science & Business Media, 2003).
[60] G. Perrotta and A. R. Jones, Unsteady forcing on a flat-plate wing in large transverse gusts, Exp. Fluids **58**, 101 (2017).
[61] A. L. Grubb, A. Moushegian, D. J. Heathcote, and M. J. Smith, Physics and computational modeling of nonlinear transverse gust encounters, in *AIAA Scitech 2020 Forum* (AIAA, Reston, VA, 2020), p. 0080.
[62] S. J. Corkery, Ph.D. thesis, University of Cambridge, 2019 (unpublished).
[63] J. Deparday and K. Mulleners, Modeling the interplay between the shear layer and leading edge suction during dynamic stall, Phys. Fluids **31**, 107104 (2019).
[64] C. Badrya, H. Biler, A. R. Jones, and J. D. Baeder, Effect of gust width on flat-plate response in large transverse gust, AIAA J. **59**, 49 (2021).
[65] S. Le Fouest, J. Deparday, and K. Mulleners, The dynamics and timescales of static stall, J. Fluids Struct. **104**, 103304 (2021).
[66] J. G. Wong and D. E. Rival, Determining the relative stability of leading-edge vortices on nominally two-dimensional flapping profiles, J. Fluid Mech. **766**, 611 (2015).